

# Sensors & Diagnostics

Accepted Manuscript

This article can be cited before page numbers have been issued, to do this please use: E. Reboli, A. Williams, A. Biswas, T. Jia, Y. Luo, M. Kumar and S. S. Iyer, *Sens. Diagn.*, 2025, DOI: 10.1039/D5SD00011D.



This is an Accepted Manuscript, which has been through the Royal Society of Chemistry peer review process and has been accepted for publication.

Accepted Manuscripts are published online shortly after acceptance, before technical editing, formatting and proof reading. Using this free service, authors can make their results available to the community, in citable form, before we publish the edited article. We will replace this Accepted Manuscript with the edited and formatted Advance Article as soon as it is available.

You can find more information about Accepted Manuscripts in the [Information for Authors](#).

Please note that technical editing may introduce minor changes to the text and/or graphics, which may alter content. The journal's standard [Terms & Conditions](#) and the [Ethical guidelines](#) still apply. In no event shall the Royal Society of Chemistry be held responsible for any errors or omissions in this Accepted Manuscript or any consequences arising from the use of any information it contains.

# Comprehensive Studies to Improve Ultrasensitive Detection of HIV-1 p24 Antigen

Evan Reboli<sup>1</sup>, Ajoke Williams<sup>1</sup>, Ankan Biswas<sup>1</sup>, Tianwei Jia<sup>2</sup>, Ying Luo,<sup>3</sup> Mukesh Kumar,<sup>4</sup> Suri Iyer<sup>1\*</sup>

<sup>1</sup>Department of Chemistry, Kennedy College of Science, University of Massachusetts Lowell, 520 Olney Science Center, Lowell, Massachusetts 01854, United States

<sup>2</sup>Department of Surgery, Beth Israel Deaconess Medical Center, Harvard Medical School, National Center for Functional Glycomics, CLS 11087-3 Blackfan Circle, Boston, Massachusetts 02115, United States

<sup>3</sup>Department of Chemistry, Center for Diagnostics and Therapeutics, Georgia State University, 788 Petit Science Center, Atlanta, Georgia 30302, United States

<sup>4</sup>Department of Biology, Center for Diagnostics and Therapeutics, Georgia State University, 622 Petit Science Center, Atlanta, Georgia 30302, United States

## Abstract

Early and accurate detection of HIV-1 p24 antigen is crucial for timely diagnosis and treatment, particularly in resource-limited settings where traditional methods often lack the necessary sensitivity for early-stage detection or is expensive. Here, we developed a layer-by-layer signal amplification platform employing fluorescent silica nanoparticles functionalized via bioorthogonal TCO/TZ chemistry. We evaluated nanoparticles of different sizes (25, 50, and 100 nm) and two dye-doped nanoparticle formulations to optimize signal intensity, detection limits, and nonspecific binding. The 25 nm RITC-doped nanoparticles demonstrated superior performance, achieving an ultra-low detection limit of 7 fg/mL with a broad linear range up to 1 ng/mL. Compared to FITC-doped nanoparticles, RITC-doped nanoparticles provided enhanced brightness and signal strength. Further optimization revealed that using 50 µg of 25 nm nanoparticles yielded the best sensitivity while minimizing nonspecific binding. This nanoparticle-based assay significantly outperformed commercial ELISA kits, offering a broad dynamic range and improved sensitivity. Our platform presents a highly sensitive and adaptable approach for HIV-1 p24 antigen detection, with broad potential applications in point-of-care diagnostics and detection of other low-abundance biomarkers, ultimately enhancing early disease detection and treatment accessibility.

**KEYWORDS:** HIV P24 Antigen, Biorthogonal, Fluorescent Silica Nanoparticles, Signal Enhancement, Broad Linear range.

## Introduction



Human Immunodeficiency Virus (HIV) remains a global health challenge, with 40 million people living with the virus, including 1.3 million newly infected individuals, according to United Nations Program on HIV/AIDS reports (UNAIDS 2023).<sup>1,2</sup> With millions of individual infected and unaware of their status, HIV testing is essential for diagnosing new infections and for monitoring the viral loads.<sup>3</sup> Therefore, it is very important to develop a detection strategy for early diagnosis and clinical treatment.<sup>4</sup>

Detection of HIV mainly relies on HIV antibodies in the blood, but in early stages these antibodies may not be present making this method less effective.<sup>5</sup> Therefore nucleic acid amplification testing (NAAT) is used to detect presence of HIV RNA.<sup>6</sup> Although advancements in mutualization and nucleic acid amplifications have been made these tests are still cost prohibitive for resource-poor areas.<sup>6,7</sup> CRISPR-based methods, while highly promising, offer rapid and sensitive HIV RNA detection but require expensive instruments, trained personnel and is cost prohibitive.<sup>8</sup> Early detection enables the prompt start of antiretroviral therapy (ART), which is crucial for controlling the viral concentration, and preventing the progression to acquired immunodeficiency syndrome (AIDS).<sup>9</sup> Children born to HIV-positive mothers can contract the virus through breast milk, making regular testing essential for the early detection of infection. Early diagnosis could help prevent this by providing timely information.<sup>10</sup> Monitoring the viral load in children with HIV is crucial for tracking disease progression and determining when to adjust antiretroviral therapies.<sup>11</sup> Fingertpick blood sampling is the most used biochip in point-of-care biomarker testing due to its minimally invasive nature, making it a practical alternative for HIV detection, particularly in low-resource settings where conducting full blood tests and utilizing hematology analyzers is not feasible.<sup>12,13</sup>



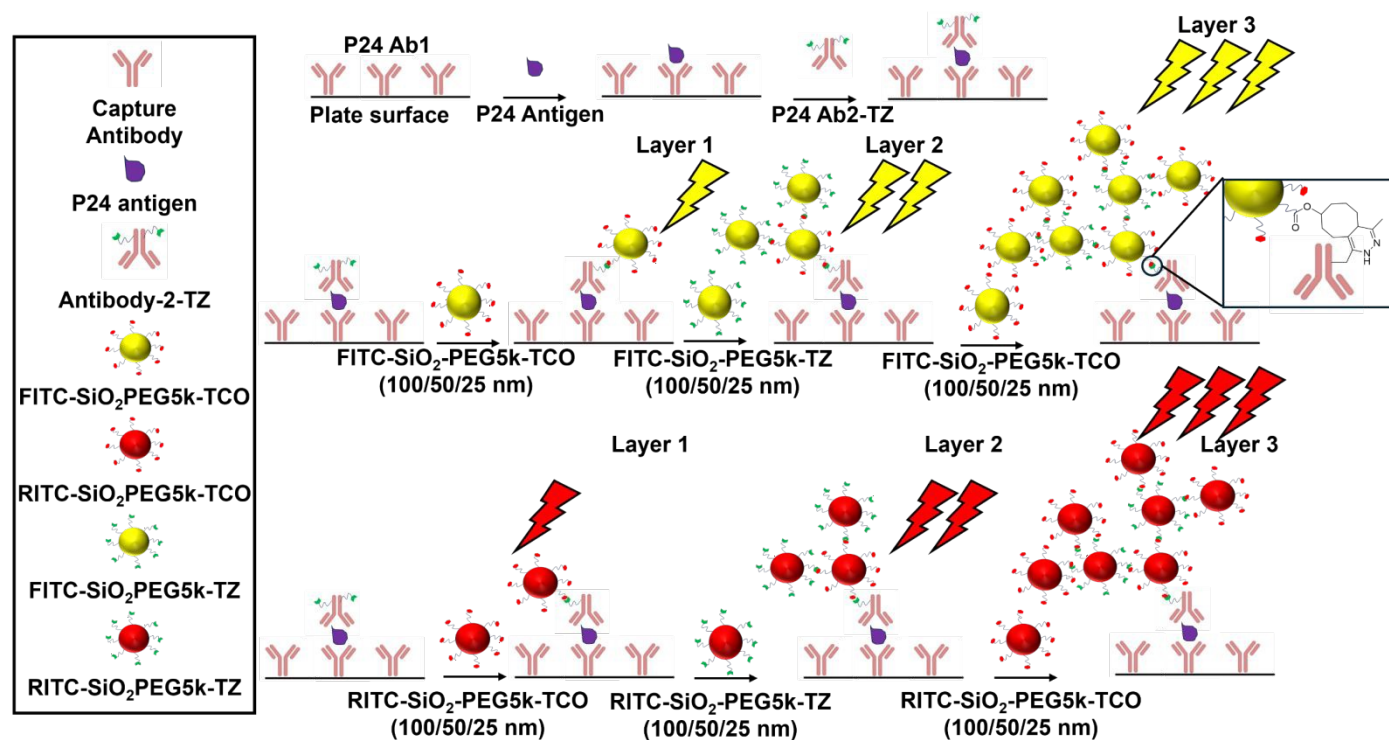


**Figure 1.** Schematic of layer-by-layer signal enhancement strategy for ultrasensitive HIV-1 p24 antigen detection using fluorescent-doped nanoparticles. Shown left are assay components, top center displays FITC-SiO<sub>2</sub>-PEG5k-TZ/TCO particles, center bottom RITC-SiO<sub>2</sub>-PEG5k-TZ/TCO particles.

HIV p24 antigen is a well-conserved structural protein within HIV and is used to monitor viral load.<sup>14</sup> p24 antigen can be detected using fourth-generation point-of-care (POC) lateral flow immunoassays approximately 15 days after HIV infection.<sup>15,16</sup> However, it remains a challenge early in infection and detecting lower concentrations. Recently, we reported an ultrasensitive p24 assay with 46 fg/mL (1.84 fM) limit of detection (LOD) and a very broad linear range spanning 8 orders of magnitude, 46 fg/mL to 10 ng/mL, utilizing a layer-by-layer fluorescent silica nanoparticles and bioorthogonal chemistries.<sup>17</sup> The signal enhancement strategy shown in **Figure 1**. First, anti-p24 antibodies are coated on the plate and blocked. Next varying concentrations of p24 are added and subsequently washed to remove unbound antigen. A secondary antibody modified with tetrazine (Ab<sub>2</sub>-TZ) is added, creating a sandwich of the antigen between two antibodies. After washing to remove excess Ab<sub>2</sub>-TZ, silica nanoparticles doped with either fluorescein isothiocyanate (FITC) or rhodamine b isothiocyanate (RITC) and functionalized with trans-cyclooctene (TCO) (FITC-SiO<sub>2</sub>-PEG5k-TCO & RITC-SiO<sub>2</sub>-PEG5k-TCO) are added to the microwell. The FITC-SiO<sub>2</sub>-PEG5k-TCO reacts with the tetrazine (TZ) conjugated to the antibody creating the first layer. Excess particles are washed leaving the first layer of bound particles, with unreacted TCO on their surfaces. The second layer is formed by the addition of the dye-doped silica nanoparticles functionalized with TZ (FITC-SiO<sub>2</sub>-PEG5k-TZ & RITC-SiO<sub>2</sub>-PEG5k-TZ), which readily reacts with unbound TCO forming the second



layer with bound TZ particles. Similar to the first layer, particles functionalized with TCO can be added to further enhance the signal.

Hence, we focused our efforts on studying the effect of (1) nanoparticles of varying sizes (25nm, 50nm, and 100nm) to potentially optimize their packing density around Ab2-TZ and (2) increasing the “brightness” of the particles by encapsulating them with a brighter dye (RITC).

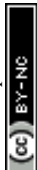
Functionalized FITC-doped nanoparticles have been extensively employed in various in vivo applications due to their exceptional photostability. Building on their success in other imaging techniques, we initially investigated their potential as signal enhancers in a novel layer-by-layer assay.<sup>18,19</sup> To further enhance signal intensity, we aimed to identify a dye with superior brightness.

The molecular brightness of a fluorophore is a critical factor in fluorescence-based applications, it is determined by the product of its molar absorptivity ( $\epsilon$ ) and fluorescence quantum yield ( $\Phi$ ), which collectively dictate the total light absorbed and the efficiency of fluorescence emission.<sup>20</sup> Consequently, we replaced FITC with Rhodamine B isothiocyanate (RITC), a rhodamine derivative with a molar absorptivity of  $106,000 \text{ M}^{-1}\text{cm}^{-1}$  and a fluorescence quantum yield of 1.06, resulting in a molecular brightness of  $112,360 \text{ M}^{-1}\text{cm}^{-1}$ .<sup>21,22</sup> This represents an approximate 20% increase in brightness compared to fluorescein derivatives, which have a molar absorptivity of  $78,000 \text{ M}^{-1}\text{cm}^{-1}$  and a quantum yield of 0.92, yielding a molecular brightness of  $71,760 \text{ M}^{-1}\text{cm}^{-1}$ .<sup>23,24</sup>

In addition to enhanced brightness, rhodamine derivatives offer several advantages over fluorescein, including longer excitation and emission wavelengths, higher quantum efficiency, and improved water solubility. Furthermore, their distinct color shifts and elevated relative fluorescence units (RFU) make them particularly valuable for fluorescence-based biosensing applications.<sup>25</sup>

## Experimental

**Materials and Equipment.** Tetraethyl orthosilicate (TEOS), 3-aminopropyl triethoxysilane (APTES), fluorescein isothiocyanate (FITC, isomer I), dimethylformamide (DMF), triethylamine (TEA), ammonium hydroxide ( $\text{NH}_4\text{OH}$ ), N-hydroxysuccinimide (NHS), 1-ethyl-3-(3-dimethylaminopropyl)carbodiimide (EDC), hydrochloric acid (HCl), sodium hydroxide (NaOH), phosphate-buffered saline (PBS), bovine serum albumin (BSA), Sulfo-NHS, Tween 20, and ethanol were purchased from Sigma-Aldrich. PEG-bis- $\text{CH}_2\text{CO}_2\text{H}$ , MW 5,000, (COOH-5k-PEG-COOH), methyltetrazine-PEG4-amine HCl salt ( $\text{Tz-PEG4-NH}_2\cdot\text{HCl}$ ), and TCO-PEG6-amine (TCO-PEG6- $\text{NH}_2$ ) were purchased from BroadPharma. The mouse anti-HIV-1 p24 paired antibody and recombinant HIV-1 p24 protein were purchased from Prospec Protein Specialists, USA. Rhodamine B isothiocyanate (RITC), and Absolute Ethanol (EtOH) were purchased from Fisher Scientific. All chemicals were



used as received without further purification. Ultrapure water obtained from a Millipore water purification system ( $18.2 \text{ M}\Omega \cdot \text{cm}^{-1}$ , Milli-Q, Merck Millipore, Darmstadt, Germany) was used in all experiments.

Zeta-potential were measured by the Horiba SZ-100 Dynamic Light Scattering (DLS) Instrument, Plates were read using the Molecular Devices Spectra Max M3 (Plate Reader), and Transmission electron microscopy (TEM) images were generated via the Philip CM12 Transmission Electron Microscope.

**Synthesis of FITC-SiO<sub>2</sub>-OH 100 nm and Fabrication of FITC-SiO<sub>2</sub>-NH<sub>2</sub>, FITC-SiO<sub>2</sub>-PEG<sub>5k</sub>-COOH, FITC-SiO<sub>2</sub>-PEG<sub>5k</sub>-TZ, FITC-SiO<sub>2</sub>-PEG<sub>5k</sub>-TCO 100 nm.** All reactions were performed under inert atmosphere as described in our previously reported paper.<sup>17</sup>

**Synthesis of FITC-SiO<sub>2</sub>-OH 50 nm nanoparticles.** FITC-SiO<sub>2</sub>-OH was prepared according to reported procedures with modifications.<sup>26</sup> In a 100 mL round-bottomed flask, FITC (10 mg) was mixed with EtOH (5 mL). APTES (20  $\mu\text{L}$ , 0.085 mmol) was added under inert conditions. The mixture was stirred for 24h at rt to yield the FITC-APTES adduct. Next absolute EtOH (50 mL), TEOS (0.75 mL, 3.36 mmol), NH<sub>4</sub>OH (30%, 2.1 mL) were added. The reaction mixture was stirred for 24h at rt. The yellow dispersion was washed with absolute EtOH (10 mL x3) through cycles of centrifugation (10,000 g, 20 min)/sonication/redispersion. Finally, the yellow nanomaterial was redispersed in absolute EtOH (10 mL). FITC-SiO<sub>2</sub>-OH was prepared in a similar manner.

**Fabrication of FITC-SiO<sub>2</sub>-NH<sub>2</sub> 50 nm nanoparticles.** The surface modification of FITC-SiO<sub>2</sub>-OH with APTES was performed in an EtOH solution at 90 °C. APTES (400  $\mu\text{L}$ , 1.7 mmol) was added to FITC-SiO<sub>2</sub>-OH (60 mg) in absolute EtOH (10 mL). The mixture was stirred for 24 h. FITC-SiO<sub>2</sub>-NH<sub>2</sub> was separated from the mixture by centrifugation (10,000  $\times$  g, 20 min) and washed with EtOH 3x. The EtOH was removed, and the material was dried *in vacuo* for 2 h.

**Fabrication of FITC-SiO<sub>2</sub>-PEG<sub>5k</sub>-COOH 50 nm nanoparticles.** HOOC-PEG<sub>5k</sub>-COOH (50 mg, 10  $\mu\text{mol}$ ) was dissolved in DMF (2 mL). EDC-HCl (2 mg, 10  $\mu\text{mol}$ ) and NHS (2 mg, 10  $\mu\text{mol}$ ) were each dissolved in DMF (400  $\mu\text{L}$ ) and added respectively. The mixture was stirred at rt for 30 min. FITC-SiO<sub>2</sub>-NH<sub>2</sub> (30 mg) was suspended in DMF (1 mL) and added to the first solution which was stirred for 24 h. The obtained nanoparticles were separated from the mixture by centrifugation (10,000  $\times$  g, 20 min) and washed with DMF 3x and EtOH 3x. The EtOH was removed, and the material was dried *in vacuo* for 2h.

**Fabrication of FITC-SiO<sub>2</sub>-PEG<sub>5k</sub>-TZ 50 nm nanoparticles.** FITC-SiO<sub>2</sub>-PEG<sub>5k</sub>-COOH (5 mg) was resuspended in DMF (1 mL). EDC-HCl (2 mg, 10  $\mu\text{mol}$ ) and NHS (2 mg, 10  $\mu\text{mol}$ ) were each dissolved in DMF





(400  $\mu\text{L}$ ) and added, respectively. The mixture was stirred at rt for 30 min. TZ-PEG<sub>6</sub>-NH<sub>2</sub> (2 mg) dissolved in DMF (200  $\mu\text{L}$ ) was added to the mixture and stirred for 24 h. The resulting nanoparticles were separated by centrifugation ( $10,000 \times g$ , 20 min), washed with EtOH (1 mL) 3x, and PBS (1 mL) 3x. The final FITC-SiO<sub>2</sub>-PEG<sub>5k</sub>-TCO nanoparticles were resuspended in PBS (5 mg/mL). The resulting stock solution was stored at 4 °C for further experimentation.

**Fabrication of RITC-SiO<sub>2</sub>-PEG<sub>5k</sub>-TCO 50 nm nanoparticles.** These nanoparticles were fabricated in a manner like the fabrication of FITC-SiO<sub>2</sub>-PEG<sub>5k</sub>-TZ using TCO-PEG<sub>6</sub>-NH<sub>2</sub> instead of TZ-PEG<sub>4</sub>-NH<sub>2</sub>.

**Fabrication of RITC-SiO<sub>2</sub>-TZ 50 nm nanoparticles.** Same protocols have followed as FITC-SiO<sub>2</sub>-TZ by using RITC (10 mg) instead of FITC (10 mg).

**Synthesis of FITC-SiO<sub>2</sub>-OH 25 nm nanoparticles.** Initially FITC (10 mg) was mixed with EtOH absolute (1 mL) and APTES (140  $\mu\text{L}$ , 0.6 mmol) in a round bottom flask under inert conditions. The mixture was stirred for 18 h forming a FITC-APTES adduct. To a flask containing EtOH (30 mL), TEOS (1.2 mL, 5.8 mmol), and NH<sub>4</sub>OH (30 % aq solution, 1.2 mL) FITC-APTES adduct quickly was added (100  $\mu\text{L}$ ). This reaction was stirred vigorously for 24 h at rt, under inert conditions. After 24 h, TEOS (240  $\mu\text{L}$ , 1.2 mmol) was added to the reaction mixture at rt under inert conditions and stirred vigorously for a further 24 h. The yellow dispersion was washed with absolute ethanol 3 x (10 mL) through cycles of centrifugation (15,000g, 25 min) / sonication/redispersion. Finally, the nano material was redispersed in EtOH (5 mL).

**Fabrication of FITC-SiO<sub>2</sub>-NH<sub>2</sub>, FITC-SiO<sub>2</sub>-PEG<sub>5k</sub>-COOH, FITC-SiO<sub>2</sub>-PEG<sub>5k</sub>-TZ, FITC-SiO<sub>2</sub>-PEG<sub>5k</sub>-TCO** were all synthesized similar manner to the 100 and 50 nm particles.

**Preparation of the Tetrazine-Modified Antibody (Ab<sub>2</sub>-TZ).** 100  $\mu\text{g}$  of p24 antibody was prepared and characterized according to previously described methods.<sup>17</sup>

**Determination of the Limit and Range of detection in PBS.** To evaluate the sensitivity of the platform, different concentrations of p24 (0.1 fg/mL – 10 ng/mL) in PBS were used. Capture antibody (3  $\mu\text{g}$ ), FITC-SiO<sub>2</sub>-PEG<sub>5k</sub>-TCO (50  $\mu\text{g}$ ), FITC-SiO<sub>2</sub>-PEG<sub>5k</sub>-TZ (50  $\mu\text{g}$ ), RITC-SiO<sub>2</sub>-PEG<sub>5k</sub>-TCO (50  $\mu\text{g}$ ), RITC-SiO<sub>2</sub>-PEG<sub>5k</sub>-TCO (50  $\mu\text{g}$ ), and Ab<sub>2</sub>-TZ (1  $\mu\text{g}$ ) were used for all analyses except concentration optimization studies. LOD was determined based on the following standard calculations  $\text{LOD} = \text{Blank (mean)} + 3 \times \text{Blank (standard deviation)}$   $\text{LOQ} = \text{Blank (mean)} + 10 \times \text{Blank (standard deviation)}$  blank), which was used to calculate the linear relationship.<sup>27</sup>



## Results and discussion

**Characterization of dye doped nanoparticles.** First, we generated all materials and characterized them meticulously. FITC and RITC dye were used to form fluorescent silica nanoparticles ranging from 100 nm, 50 nm, and 25 nm as described.<sup>26,28</sup> TEM images (**Figure 2**) unequivocally confirmed the uniformity of nanoparticle size, which was further quantified using ImageJ to generate size distribution histograms (**Figure 3**), demonstrating the expected frequency of the target diameters. The particles surface of the nanoparticles was then modified with a polyethylene glycol spacer terminated with a carboxylic group to reduce nonspecific binding. Next, TCO or TZ was conjugated to the fluorescent silica nanoparticles by first activating the surface with EDC/NHS, followed by the addition of NH<sub>2</sub>-PEG-TCO or NH<sub>2</sub>-PEG-TZ. This process resulted in the formation of FITC-SiO<sub>2</sub>-PEG5k-TCO or FITC-SiO<sub>2</sub>-PEG5k-TZ, respectively.

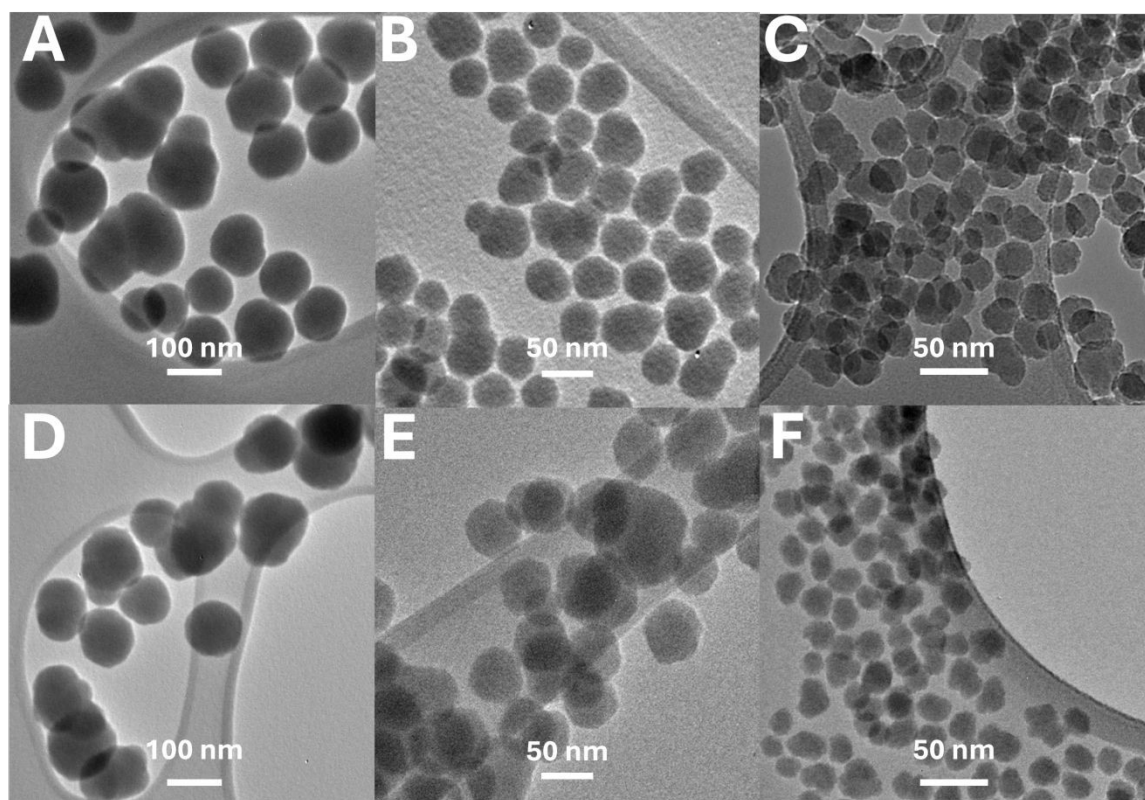


**Figure 2.** TEM images of (A) 100 nm FITC-SiO<sub>2</sub>-OH, (B) 50 nm FITC-SiO<sub>2</sub>-OH, (C) 25 nm FITC-SiO<sub>2</sub>-OH, (D) 100 nm RITC-SiO<sub>2</sub>-OH, (E) 50 nm RITC-SiO<sub>2</sub>-OH, (F) 25 nm RITC-SiO<sub>2</sub>-OH

Zeta potential measurements were used throughout the surface modification process of the fluorescent silica nanoparticles to confirm the success of each modification step and assess surface charge, a technique commonly





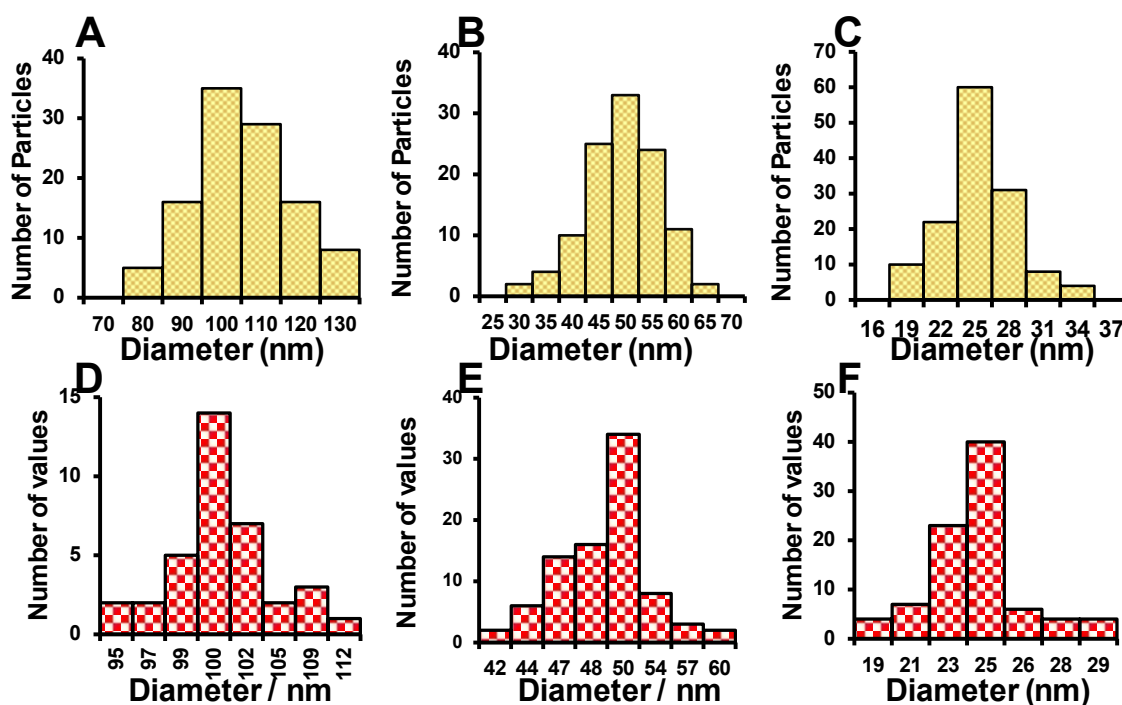


**Figure 3.** Size distribution of (A) 100 nm FITC-SiO<sub>2</sub>-OH, (B) 50 nm FITC-SiO<sub>2</sub>-OH, (C) 25 nm FITC-SiO<sub>2</sub>-OH, (D) 100 nm RITC-SiO<sub>2</sub>-OH, (E) 50 nm RITC-SiO<sub>2</sub>-OH, (F) 25 nm RITC-SiO<sub>2</sub>-OH.

applied in related studies such as fluorescence immunoassays on paper and bio responsive quantum dot-enzyme platforms.<sup>29,30</sup> Different surface chemistries exhibit varying surface potential charges, with the zeta potential of the dye-doped SiO<sub>2</sub>-OH particles initially ranging from −25 mV to −9 mV, attributed to the presence of hydroxyl groups on the surface, as shown in **Figure 4**. Upon coating the surface with amine functional groups, the zeta potential shifted to a positive range of +9 to +15 mV, clearly indicating the successful addition of the amine group. Next, bis-carboxylic PEG linker was conjugated to the surface, where the zeta potential ranged from -9 to -3 mV. Finally, the addition of TZ or TCO functionalities caused a dip in the zeta potential rendering it slightly negative



which reflects the final modification.

**Functional and photostability.** We evaluated the performance of each dye doped fluorescent silica nanoparticles at the same weight concentration. Next the excitation and emission spectra of equivalent weighted particles was measured and compared (**Figure S1-2**) for RITC and FITC. The results showed that nanoparticles with a size of 100 nm exhibited the highest intensity, where 25 nm particles were the lowest intensity, all things being equal (**Figure S3**).

To ensure robustness we measured photostability and the functional stability of the TCO/TZ modified particles. Photostability studies show the particle fluorescence intensity remains stable over a month (**Figure S2**). Functional stability studies were conducted to assess the stability of TCO- and TZ-functionalized particles. Three concentrations of p24 antigen—control, 100 fg/mL, and 1 ng/mL were analyzed weekly to determine any changes

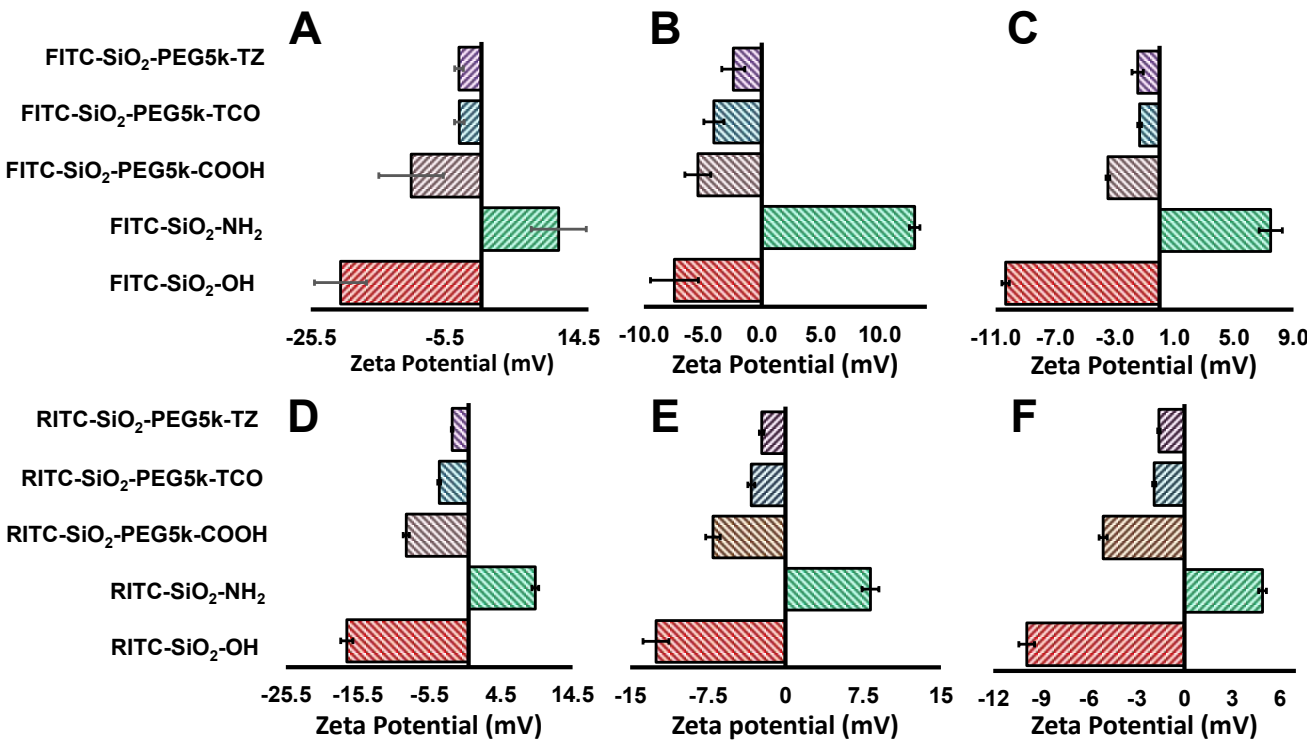


**Figure 4.** Zeta potentials of fluorescent silica nanoparticles (A) FITC-SiO<sub>2</sub>-R 100 nm, (B) FITC-SiO<sub>2</sub>-R 50 nm, (C) FITC-SiO<sub>2</sub>-R 25 nm, (D) RITC-SiO<sub>2</sub>-R 100 nm, (E) RITC-SiO<sub>2</sub>-R 50 nm, (F) RITC-SiO<sub>2</sub>-R 25 nm. Error bars indicate the standard deviation of three measurements.

in performance trends. While a nonspecific binding increase was observed over the experiment, the overall trend in detection remained for three weeks. (**Figure S3**).

**Concentration optimization studies.** To evaluate the optimal concentration of 50 nm fluorescent-doped nanoparticles for assay sensitivity, we tested three concentrations: 25 µg, 50 µg, and 75 µg of FITC-SiO<sub>2</sub>-TZ/TCO

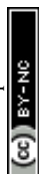
particles. At 25  $\mu\text{g}$  (**Figure 4A**), the assay achieved a limit of detection (LOD) of 150 fg/mL and a limit of quantification (LOQ) of 4 pg/mL, with a linear range of 150 fg/mL to 1 ng/mL. This concentration resulted in low non-specific binding and reduced variability but exhibited weaker signal intensity due to the limited number of particles. Increasing the concentration to 50  $\mu\text{g}$  of particles (**Figure 4B**) enhanced the LOD to 66 fg/mL and the LOQ to 1 pg/mL, with a linear range of 66 fg/mL to 1 ng/mL. This concentration provided an optimal balance between signal strength and non-specific binding, despite moderate levels of the latter. Further increasing the concentration to 75  $\mu\text{g}$  (**Figure 4C**) resulted in an excess of particles, raising the LOD significantly to 500 pg/mL and diminishing assay sensitivity. Therefore, 50  $\mu\text{g}$  was identified as the optimal concentration, offering the best trade-off between signal strength and non-specific binding.

**Packing optimization studies.** We hypothesized that smaller nanoparticles would improve packing efficiency, as illustrated in **Figure 5**. To estimate packing density, we calculated the binding capacity of a 96-well plate (**Table 1**), assuming 400–500 ng of IgG antibody can bind per  $\text{cm}^2$  of the plate's surface area. For a 24 kDa p24 antibody (Ab1), this corresponds to approximately  $1.0 \times 10^{13}$  to  $1.25 \times 10^{13}$  antibodies per  $\text{cm}^2$ , or  $3.2 \times 10^{12}$  antibodies per well, based on a binding density of 400 ng/ $\text{cm}^2$ . The concentration range of p24 antigen in each well (200  $\mu\text{L}$ ) spans from 0.1 fg/mL to 10  $\mu\text{g/mL}$ , translating to approximately  $5.0 \times 10^2$  to  $5.0 \times 10^{16}$  antigens per well.

Using TEM analysis, we estimated approximately  $6.7 \times 10^7$  dye-doped 50 nm particles per 1  $\mu\text{g}$ . With an estimated particle binding area of  $5.67 \times 10^{-10} \text{ cm}^2$  and a total well surface area of 0.32  $\text{cm}^2$ , the maximum particle binding capacity in a single layer was calculated to be  $2.22 \times 10^9$  particles, equivalent to 33  $\mu\text{g}$  of particles. These calculations underscore the importance of selecting appropriately sized nanoparticles and their concentrations to maximize assay sensitivity and minimize non-specific interactions. Layer-by-layer attachment of the particles are shown in confocal images (**Figure S5**). Increasing brightness of the particles are clearly visible in 2<sup>nd</sup> and 3<sup>rd</sup> layer.

**Size comparison studies.** Size comparison studies were performed, as shown in **Figure 6**, with the hypothesis that smaller particles would yield a lower limit of detection (LOD) due to improved packing of the layers. Starting with 100 nm FITC-doped particles (**Figure 6A**), we reduced the particle size to 50 nm (**Figure 6B**), and finally to 25 nm (**Figure 6C**). The LOD decreased from 163 fg/mL for the 100 nm particles to 66 fg/mL for the 50 nm particles, and further to 13 fg/mL for the 25 nm particles.

Similarly, the RITC-doped particles (**Figure 6D-F**) exhibited a comparable trend, where particle size inversely affected the LOD. The 100 nm RITC-doped particles showed an initial LOD of 50 fg/mL, which decreased to 42 fg/mL with the 50 nm particles, and 7 fg/mL with the 25 nm particles. These results, along with the extended



linear range, are summarized in **Table 2**. Notably, the linear range extended from 7 fg/mL to 1 ng/mL with the 25 nm RITC-doped particles.

**Dye comparison studies.** When comparing dyes to dyes regardless of particle size we see that RITC-doped particles vastly outperform their FITC counterparts, this is likely due to the increase “brightness” of the fluorophore. We see this trend repeated in 100 nm FITC and 100 nm doped RITC particles in **Figure 6 A & D** respectively, 50 nm FITC and 50 nm doped RITC particles in **Figure 6 B & E** respectively, and for the 25 doped particles in **Figure 6 C & F**.

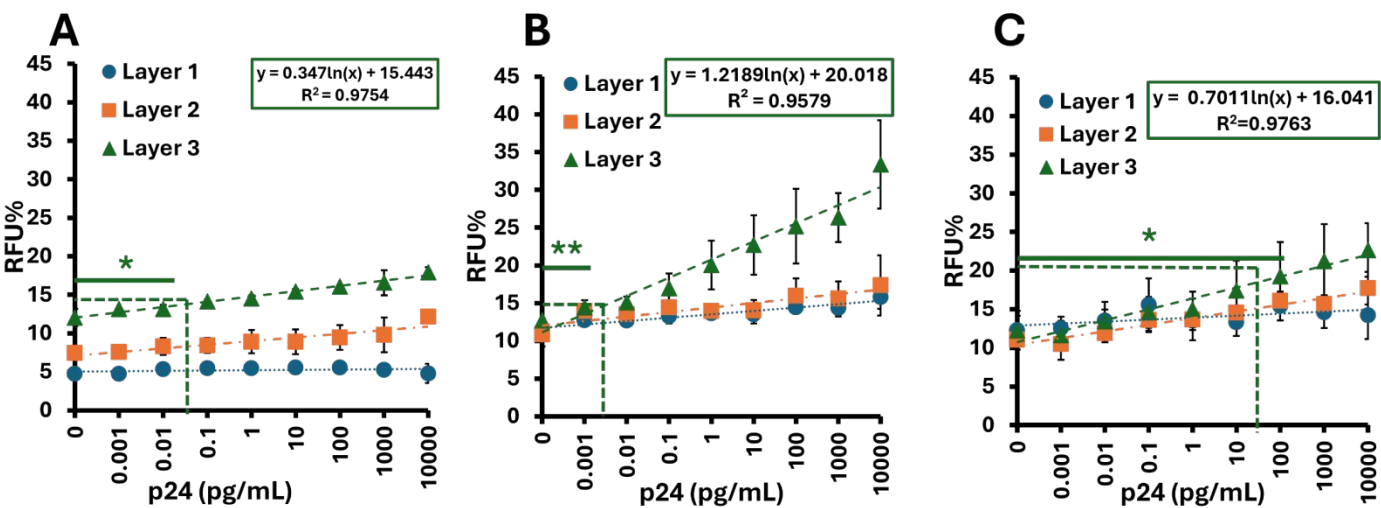


**Figure 5.** Studies of different weight concentrations of 50 nm particles the signal value and different concentrations of p24 antigen, concentration optimization for 50 nm FITC-SiO<sub>2</sub>-TCO/TZ (A) 25ug (B) 50 ug (C) 75 ug. The y-axis, %RFU, is the percent relative fluorescence intensity of the sample as a function of an internal control. Error bars indicate the standard deviations of three measurements. (ns>0.05, \*p <0.05.)

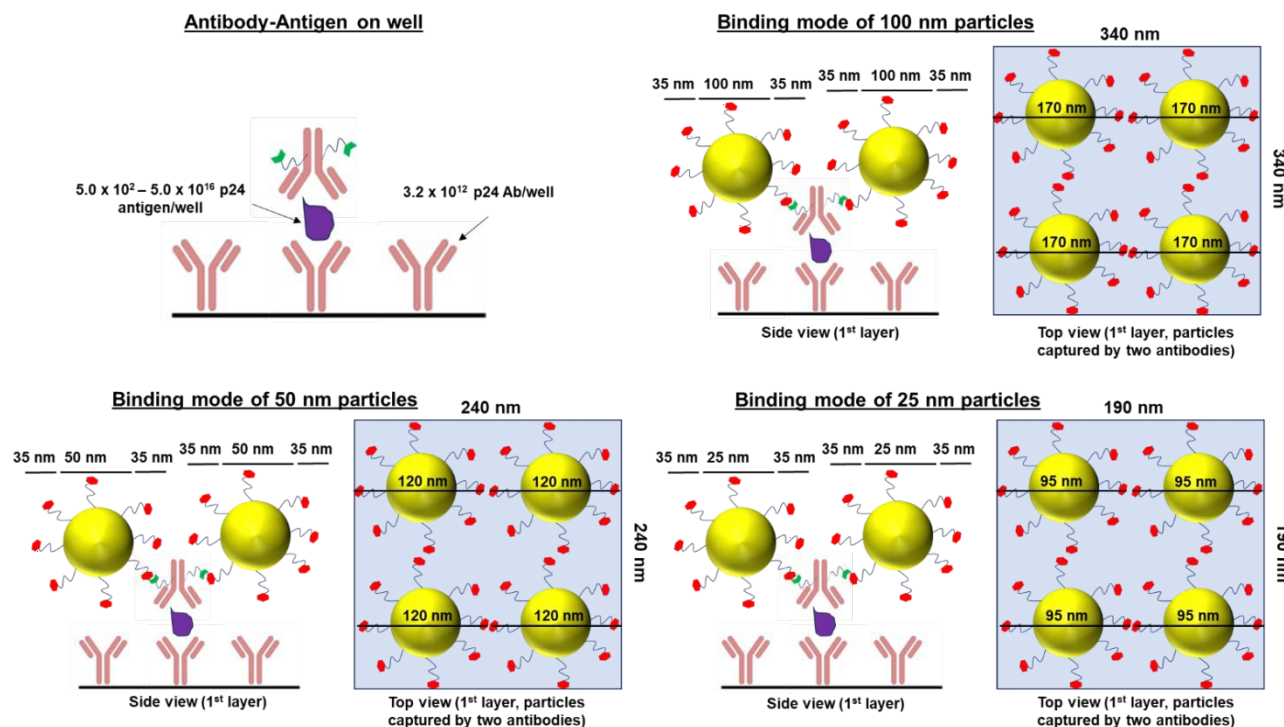


**Figure 6** Theoretical packing density calculation of different sized (100 nm, 50 nm, and 25 nm) nanoparticles and number of Antigen and Antibody per well of 96 well plate during the assay.

**Table 1** Quantification of nanoparticles

Entry	100 nm	50 nm	25 nm
Area covered by 4 particles (A1)	$1.156 \times 10^{-9} \text{ cm}^2$	$5.76 \times 10^{-10} \text{ cm}^2$	$3.61 \times 10^{-10} \text{ cm}^2$
Surface area of well (A2)	$0.32 \text{ cm}^2$	$0.32 \text{ cm}^2$	$0.32 \text{ cm}^2$
Average length of PEG5k	35 nm	35 nm	35 nm
Max NPs fit in 1 <sup>st</sup> layer {N1 = 4(A2/A1)}	$1.10 \times 10^9$	$2.22 \times 10^9$	$3.55 \times 10^9$
No of NPs in 1 $\mu\text{g}$ (N2)	$1.5 \times 10^7$	$6.7 \times 10^7$	$1.65 \times 10^8$
NPs required ( $\mu\text{g}$ ) to cover the well surface (N1/N2)	73 $\mu\text{g}$	33 $\mu\text{g}$	21 $\mu\text{g}$

**Comparison with standard ELISA.** To benchmark the performance of our novel assay, we conducted a direct comparison with a commercially available ELISA kit (Human, Mouse, & Rat HIV-1 Gag p24 ELISA Kit -





Quantikine, R&D Systems), which was enhanced with Amplex™ Red and Amplex™ UltraRed fluorescent substrates to align with the fluorescence-based nature of our method. The commercial ELISA demonstrated a linear range of 7.8–500 pg/mL and a limit of detection (LOD) of 3.35 pg/mL as seen in **Figure 9A**. In contrast, our layer-by-layer amplification assay, incorporating 25 nm RITC-doped nanoparticles, exhibited a markedly superior performance with an LOD of 7 fg/mL and an extended linear range of 0.0072–1 ng/mL in layer 3 (**Figure 9B**). Our assay offers over eight orders of magnitude greater sensitivity and a broader dynamic range than the commercial ELISA. Furthermore, as shown in **Table 3**, a direct comparison of our assay with other bioanalytical sensors for p24 demonstrates that our platform achieves superior sensitivity and an unmatched linear range.

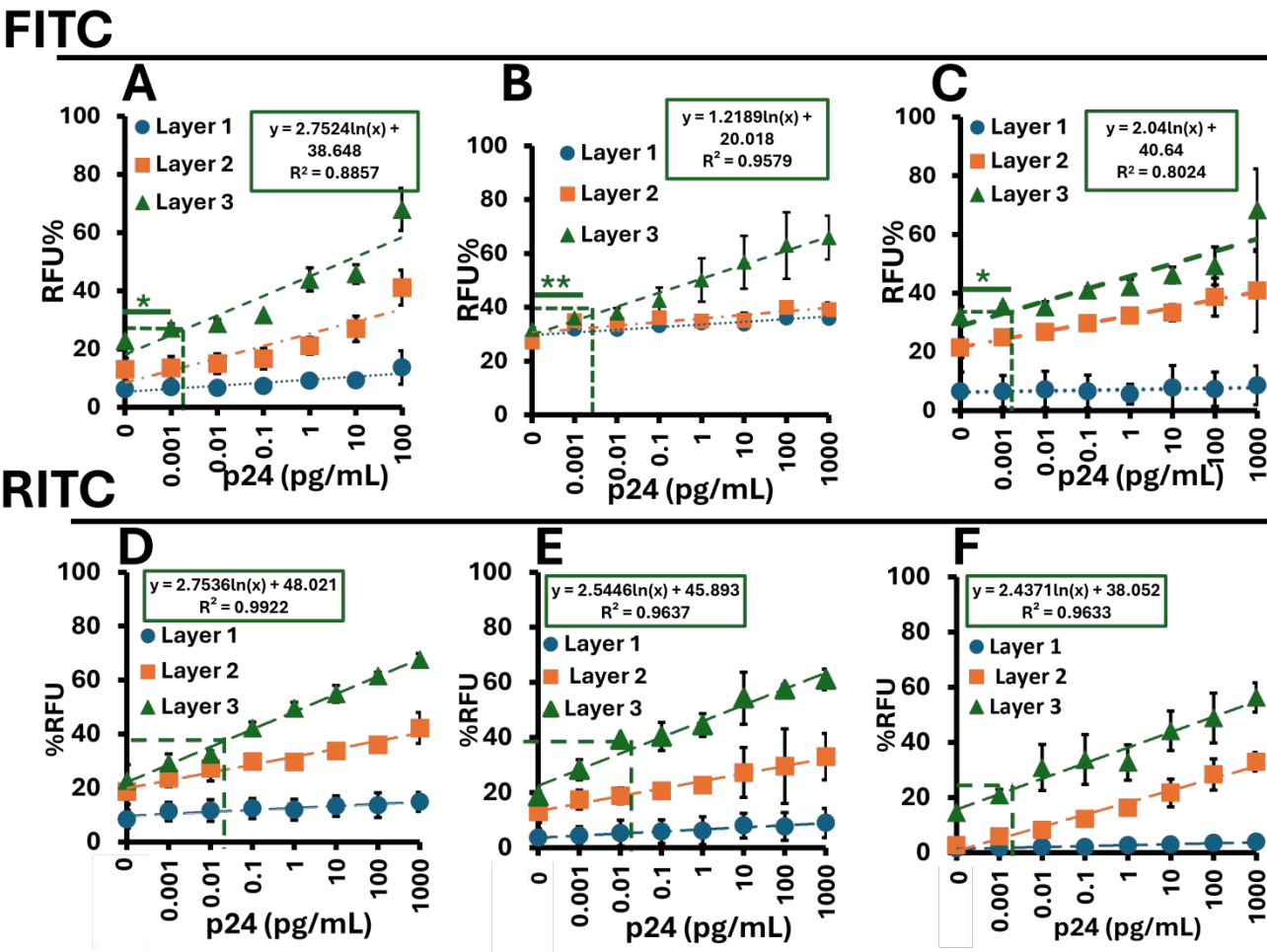


**Figure 7.** Signal Response of the sandwich immunoassay using multiple layers. (A) FITC 100 nm, (B) FITC 50 nm, (C) FITC 25 nm, (D) RITC 100 nm, (E) RITC 50 nm, (F) RITC 25 nm. The y-axis, % RFU, is the percent of relative fluorescence intensity of the sample as a function of an internal control. Error bars indicate the standard

**Table 3.** Comparison of analytical sensitivity to other P24 biosensors

Detection Methods	Strategy	LOD	Detection Range	Reference	Year
Fluorescence	streptavidin-conjugated AuNCs	5.0 pg/mL	Up to 1000 pg/mL	31	2018
Fluorescence and visual	TdT, CuNPs	0.025 fg/mL	0.025–1000 fg/mL	32	2022
LFIA-naked eye	PtNCs, CN/DAB	0.8 pg/mL	0.8–10,000 pg/mL	33	2018
Fluorescence	streptavidin labeled FSN	8.2 pg/mL	8.2–1000 pg/mL	34	2017
Fluorescence	$\beta$ -sheets bind with Congo red	0.61 pg/mL (3F-based) 2.44 pg/mL (2F-based)	0.61–150 pg/mL 2.44–150 pg/mL	34	2020
PEC	ALP-encapsulated liposomes	0.63 pg/mL	0.63–50,000 pg/mL	36	2018
Electrochemical	Fe <sub>3</sub> O <sub>4</sub> @SiO <sub>2</sub> Ab1/AuNPs/EV-p24 Ab2	0.5 pg/mL	0.5–10,000 pg/mL	37	2013
Fluorescence	layer-by-layer signal amplification	0.017 pg/mL (PBS) 0.046 pg/mL (serum)	0.017–10,000 pg/mL 0.046–10,000 pg/mL	17	2024
Fluorescence	layer-by-layer signal amplification	0.007 pg/mL	0.007–10,000 pg/mL	This Work	2024

**Table 2.** Summary of assay results

Nanoparticle type	LOD (fg/mL)	Linear range	Linearity (R <sup>2</sup> )
100nm FITC	163	0.163–1ng/mL	0.86
50nm FITC	66	0.0066–1ng/mL	0.98
25nm FITC	13	0.0013–1ng/mL	0.81
100nm RITC	50	0.0504–1ng/mL	0.99
50nm RITC	42	0.0420–1ng/mL	0.96
25nm RITC	7	0.0072–1ng/mL	0.94



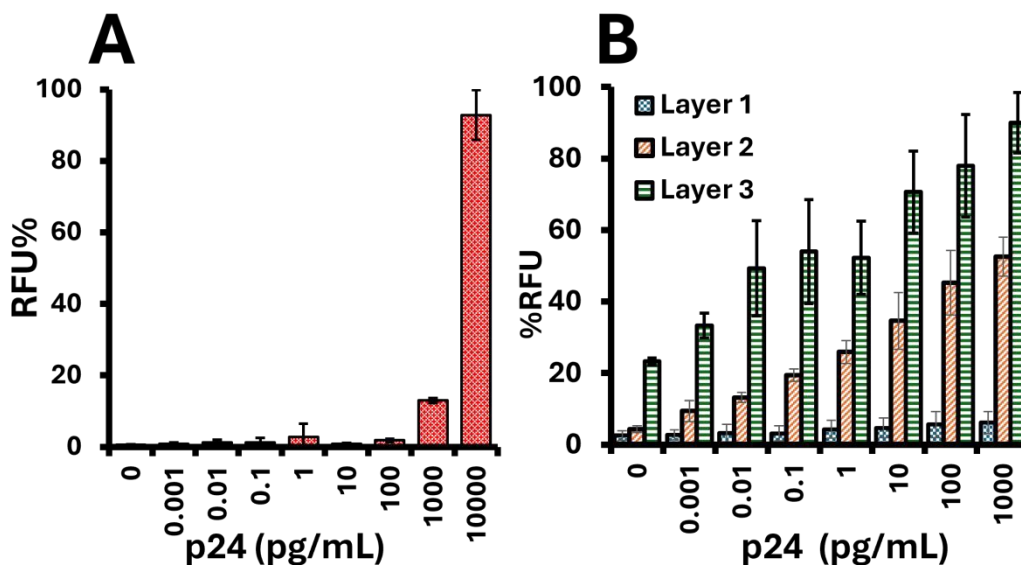


**Figure 8.** Comparison of Detection Sensitivity: (A) Commercially available ELISA for HIV p24 antigen detection and (B) enhanced layer-by-layer amplification assay using 25 nm RITC-doped nanoparticles, highlighting the improved sensitivity and linear range of our method.

## Conclusions

We successfully synthesized and characterized FITC- and RITC-doped silica nanoparticles ranging in size from 25 nm, 50nm, and 100 nm. Particle sizes were confirmed via TEM, while Image J analyses and zeta potential measurements validated surface modifications, including the addition of polyethylene glycol spacers and TCO or TZ functionalities. These nanoparticles were employed in an extensive comparative study to enhance the ultrasensitive detection of the HIV-1 p24 antigen. By leveraging bioorthogonal chemistries and advanced signal amplification techniques, we optimized their detection capabilities for improved sensitivity in point-of-care applications. Our bioorthogonal layer-by-layer approach differs from conventional multivalent binding (e.g., streptavidin-biotin) by reducing steric hindrance and enhancing binding kinetics, improving target accessibility and signal amplification. This is because we are using two small molecules that are much smaller in size compared to avidin, which is a protein. The advancement of multifunctional nanoparticles in diagnostics can significantly benefit from the use of mutually orthogonal combinations.<sup>38</sup>

RITC-doped nanoparticles consistently outperformed FITC-doped counterparts, offering superior signal enhancement, due to improved molecular brightness. Our findings further validated that smaller nanoparticles enhance packing density, significantly lowering the limits of detection (LOD). Notably, the 3<sup>rd</sup> layer of 25 nm RITC-doped nanoparticles demonstrated a LOD of 7 fg/mL and an extended linear range from 7 fg/mL to 1



ng/mL. —eliminating the need for sample dilution, even with highly concentrated specimens. This broad linear range spanning seven orders of magnitude simplifies sample preparation, reduces the risk of dilution errors, and makes the assay more user-friendly and efficient. Beyond HIV-1 p24 antigen detection, these developments demonstrate the platform's potential for diverse diagnostic applications requiring sensitive detection of low analyte concentrations. The method offers a broad linear range that eliminates the need for sample dilution when detecting multiple biomarkers. However, challenges remain, including limited nanoparticle stability (3 weeks at rt and the requirement for multiple wash steps, which can increase assay complexity and time. We are actively working to improve nanoparticle stability and streamline the process for point-of-care diagnostics.

## Author information

### Corresponding Author

**Suri Iyer** – 520 Department of Chemistry, Kennedy College of Science, University of Massachusetts Lowell, 520 Olney Science Center, Lowell, Massachusetts 01854, United States

Sure\_iyer@uml.edu

### Authors

**Evan Reboli** - Department of Chemistry, Kennedy College of Science, University of Massachusetts Lowell, 520 Olney Science Center, Lowell, Massachusetts 01854, United States

**Ajoke Williams** - Department of Chemistry, Kennedy College of Science, University of Massachusetts Lowell, 520 Olney Science Center, Lowell, Massachusetts 01854, United States

**Ankan Biswas** - Department of Chemistry, Kennedy College of Science, University of Massachusetts Lowell, 520 Olney Science Center, Lowell, Massachusetts 01854, United States

**Jia Tianwei** - Department of Surgery, Beth Israel Deaconess Medical Center, Harvard Medical School, National Center for Functional Glycomics, CLS 11087-3 Blackfan Circle, Boston, Massachusetts 02115, United States

### Acknowledgements

We are grateful for to the National Institute of Allergy and Infectious Diseases (grant no.5R61AI140475). We would also like to express our gratitude to the UMass Lowell Core Research Facilities for their invaluable support throughout this project. Special thanks to Wendy Gavin for her expert assistance with the Dynamic Light



Scattering Instrument (Horiba SZ-100) and to Anna Maria Routsis for her guidance and help with the TEM imaging. Their expertise greatly contributed to the success of our work.

## References

- 1 UNAIDS, Global HIV & AIDS statistics — Fact sheet, 2024.
- 2 S. Payagala and A. Pozniak, *Update Dermatol. Asp. STD HIV*, 2024, **42**, 119–127.
- 3 M. Wu, B. Yang, L. Shi, Q. Tang, J. Wang, W. Liu, B. Li and Y. Jin, *Anal. Chim. Acta*, 2024, **1304**, 342553.
- 4 E. M. Girardi, C. A. P. Sabin and A. d'Arminio M. Monforte, *JAIDS J. Acquir. Immune Defic. Syndr.*, 2007, **46**, S3.
- 5 G. Pantaleo, B. Correia, C. Fenwick, V. S. Joo and L. Perez, *Nat. Rev. Drug Discov.*, 2022, **21**, 676–696.
- 6 P. Patel, D. Mackellar, P. Simmons, A. Uniyal, K. Gallagher, B. Bennett, T. J. Sullivan, A. Kowalski, M. M. Parker, M. LaLota, P. Kerndt, P. S. Sullivan, and Centers for Disease Control and Prevention Acute HIV Infection Study Group, *Arch. Intern. Med.*, 2010, **170**, 66–74.
- 7 S. Tian, L. Huang, Y. Gao, Z. Yu and D. Tang, *Sens. Diagn.*, 2023, **2**, 707–713.
- 8 N. Uno, Z. Li, L. Avery, M. M. Sfeir and C. Liu, *Anal. Chim. Acta*, 2023, **1262**, 341258.
- 9 T. Liu, A. J. Politza, A. Kshirsagar, Y. Zhu and W. Guan, *ACS Sens.*, 2023, **8**, 4716–4727.
- 10 L. Abuogi, L. Noble and C. Smith, *Pediatrics*, 2024, **153**, e2024066843.
- 11 K. A. Veldsman, B. Laughton, A. Janse van Rensburg, P. Zuidewind, E. Dobbels, S. Barnabas, S. Fry, M. F. Cotton and G. U. van Zyl, *AIDS*, 2021, **35**, 1247.
- 12 M. M. Bond and R. R. Richards-Kortum, *Am. J. Clin. Pathol.*, 2015, **144**, 885–894.
- 13 E. Cheah, D. P. Tran, M. T. Amen, R. D. Arrua, E. F. Hilder and B. Thierry, *Anal. Chem.*, 2022, **94**, 1256–1263.
- 14 S. Tang, J. Zhao, A. Wang, R. Viswanath, H. Harma, R. F. Little, R. Yarchoan, S. L. Stramer, P. N. Nyambi, S. Lee, O. Wood, E. Y. Wong, X. Wang and I. K. Hewlett, *Clin. Vaccine Immunol.*, 2010, **17**, 1244–1251.
- 15 N. E. Rosenberg, C. D. Pilcher, M. P. Busch and M. S. Cohen, *Curr. Opin. HIV AIDS*, 2015, **10**, 61.
- 16 E. R. Gray, R. Bain, O. Varsaneux, R. W. Peeling, M. M. Stevens and R. A. McKendry, *AIDS Lond. Engl.*, 2018, **32**, 2089–2102.
- 17 T. Jia, V. Saikam, Y. Luo, X. Sheng, J. Fang, M. Kumar and S. S. Iyer, *ACS Omega*, 2024, **9**, 14604–14612.
- 18 K. Wang, X. He, X. Yang and H. Shi, *Acc. Chem. Res.*, 2013, **46**, 1367–1376.
- 19 C. Xie, D. Yin, J. Li, L. Zhang, B. Liu and M. Wu, *Nano Biomed. Eng.*, 2009, **1**, 27–31.
- 20 A. H. Ashoka, I. O. Aparin, A. Reisch and A. S. Klymchenko, *Chem. Soc. Rev.*, 2023, **52**, 4525–4548.
- 21 L. D. Lavis and R. T. Raines, *ACS Chem. Biol.*, 2008, **3**, 142–155.
- 22 J. B. Grimm and L. D. Lavis, *Nat. Methods*, 2022, **19**, 149–158.
- 23 J. B. Grimm, B. P. English, J. Chen, J. P. Slaughter, Z. Zhang, A. Revyakin, R. Patel, J. J. Macklin, D. Normanno and R. H. Singer, *Nat. Methods*, 2015, **12**, 244–250.
- 24 I. McKay, D. Forman and R. White, *Immunology*, 1981, **43**, 591.
- 25 H. N. Kim, M. H. Lee, H. J. Kim, J. S. Kim and J. Yoon, *Chem. Soc. Rev.*, 2008, **37**, 1465–1472.
- 26 M. L. Vera, A. C  nneva, C. Huck-Iriart, F. G. Requejo, M. C. Gonzalez, M. L. Dell'Arciprete and A. Calvo, *J. Colloid Interface Sci.*, 2017, **496**, 456–464.
- 27 S.-W. Lin, C.-F. Shen, C.-C. Liu and C.-M. Cheng, *Front. Bioeng. Biotechnol.*, 2021, **9**, 752681.
- 28 G. Durgun, K. Ocakoglu and S. Ozelik, *J. Phys. Chem. C*, 2011, **115**, 16322–16332.
- 29 S. Lv, Y. Tang, K. Zhang and D. Tang, *Anal. Chem.*, 2018, **90**, 14121–14125.
- 30 Z. Qiu, J. Shu and D. Tang, *Anal. Chem.*, 2017, **89**, 5152–5160.
- 31 A. D. Kurdekar, L. A. Avinash Chunduri, C. S. Manohar, M. K. Haleyurgirisetty, I. K. Hewlett and K. Venkataramaniah, *Sci. Adv.*, 2018, **4**, eaar6280.





- 32 P. Chen, Z. Tang, K. Huang, Y. Wei, D. Li, Y. He, M. Li, D. Tang, Y. Bai, Y. Xie, J. Huang, C. Tao and B. Ying, *Sens. Actuators B Chem.*, 2022, **354**, 131209.
- 33 C. N. Loynachan, M. R. Thomas, E. R. Gray, D. A. Richards, J. Kim, B. S. Miller, J. C. Brookes, S. Agarwal, V. Chudasama, R. A. McKendry and M. M. Stevens, *ACS Nano*, 2018, **12**, 279–288.
- 34 A. D. Kurdekar, L. A. A. Chunduri, S. M. Chelli, M. K. Haleyurgirisetty, E. P. Bulagonda, J. Zheng, I. K. Hewlett and V. Kamisetti, *RSC Adv.*, 2017, **7**, 19863–19877.
- 35 H. Cao, Y. Liu, H. Sun, Z. Li, Y. Gao, X. Deng, Y. Shao, Y. Cong and X. Jiang, *Anal. Chem.*, 2020, **92**, 11089–11094.
- 36 J. Zhuang, B. Han, W. Liu, J. Zhou, K. Liu, D. Yang and D. Tang, *Biosens. Bioelectron.*, 2018, **99**, 230–236.
- 37 N. Gan, X. Du, Y. Cao, F. Hu, T. Li and Q. Jiang, *Materials*, 2013, **6**, 1255–1269.
- 38 W. R. Algar, D. E. Prasuhn, M. H. Stewart, T. L. Jennings, J. B. Blanco-Canosa, P. E. Dawson and I. L. Medintz, *Bioconjug. Chem.*, 2011, **22**, 825–858.



- The data supporting this article have been included as part of the Supplementary Information.

